High-order Total Variation Regularization Approach for Axially Symmetric Object Tomography from a Single Radiograph

Raymond H. Chan,[*] Haixia Liang,[†] Suhua Wei,[‡] Mila Nikolova,[§] and Xue-Cheng Tai [¶]

Abstract

In this paper, we consider tomographic reconstruction for axially symmetric objects from a single radiograph formed by fan-beam X-rays. All contemporary methods are based on the assumption that the density is piecewise constant or linear. From a practical viewpoint, this is quite a restrictive approximation. The method we propose is based on high-order total variation regularization. Its main advantage is to reduce the staircase effect while keeping sharp edges and enable the recovery of smoothly varying regions. The optimization problem is solved using the augmented Lagrangian method which has been recently applied in image processing. Furthermore, we use a one-dimensional (1D) technique for fan-beam X-rays to approximate 2D tomographic reconstruction for cone-beam X-rays. For the 2D problem, we treat the cone beam as fan beam located at parallel planes perpendicular to the symmetric axis. Then the density of the whole object is recovered layer by layer. Numerical results in 1D show that the proposed method has improved the preservation of edge location and the accuracy of the density level when compared with several other contemporary methods. The 2D numerical tests show that cylindrical symmetric objects can be recovered rather accurately by our high-order regularization model.

Key words: Tomography, Radiograph, Abel inversion, High-order total variation, Augmented Lagrangian method,

1   Introduction

The X-ray tomography has been widely applied in many areas, including medicine, optics, material science, astronomy, and geophysics. Another important application of X-ray tomography is in nuclear physics. In this paper, we focus on the problem of tomographic reconstruction for flash X-ray radiography. The purpose here is to characterize the state of matter subjected to powerful

shocks under the effect of explosives. By tomographic reconstruction we aim to recover the object density.

In our experimental setting, the object is assumed axially symmetric. Only a single radiograph is taken with a radiographic axis perpendicular to the symmetric axis of the object. The diagram for the experiment is depicted on Figure 1(a) where the symmetric axis of the object is defined as the z-axis. The X-ray source is placed sufficiently far from the object compared to its size, so that the X-rays can be assumed to be parallel on different layers. The object density is reconstructed layer by layer independently. In each layer, i.e. for each constant z, we consider that the X-rays form a fan-beam shape, see Figure 1(b). The transmitted radiation is measured by a detector lying on a plane $x = x_0$. Each cross section of the object is projected onto a line of the detector plane.
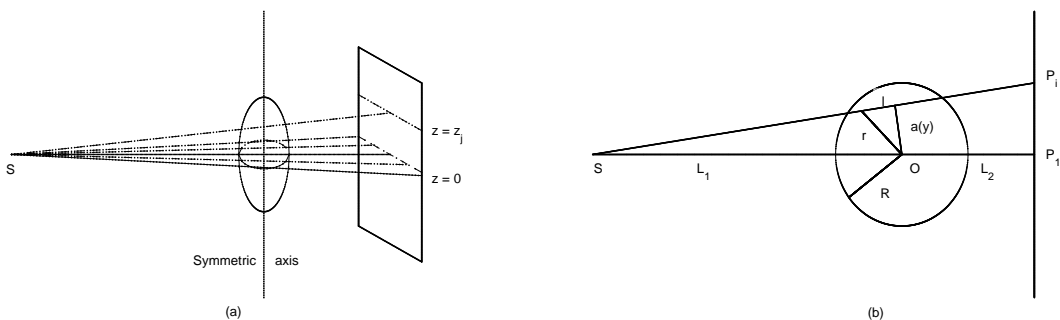

Figure 1: Illustration to the tomographic experiments in (a) 2D and (b) 1D.

In flash radiography, a very high photon energy is emitted so that it passes through the object. The X-ray energy is attenuated after absorption by the object. The absorption depends on the nature, density, and thickness of the materials contained in the object. The logarithm of the attenuation is regarded proportional to the integral of the density function of the object along the X-ray beam path. For the tomographic reconstruction we will assume that the integral value of density function is known. In each cross section, the density function is one dimensional, denoted by $\rho(r, z)$. The integral $\int \rho(r, z) \mathrm{d}l$ along each line through the object is given by the radiograph intensity $d(y, z)$. For simplicity, in the following part we will use $d(y)$ and $\rho(r)$ to respectively represent the radiograph intensity and object density for any cross section for each fixed z. The relationship between r, l and $a(y)$ reads

$$l^2 = r^2 - a(y)^2,$$

where $a(y)$ is the distance from the center of the cross section to the corresponding X-ray. Introducing the latter equation into $d(y) = \int \rho(r) \mathrm{d}l$ yields

$$d(y) = 2 \int_{|a(y)|}^{R} \frac{r\rho(r)}{\sqrt{r^2 - a(y)^2}} \mathrm{d}r, \tag{1.1}$$

which is the Abel transform of ρ. Let us remind that the Abel transform is the 1D version of the usual Radon transform.

Solving $\rho(r)$ from (1.1) amounts to invert the Abel transform. In practice, there are a number of difficulties to address the Abel transform based tomography. First, (1.1) is a simplified description of a very nonlinear experimental process where all the measurements are subject to noise. Second,

the inverse problem is ill-posed. It makes the corresponding discrete Abel transform very ill-conditioned. In the discrete setting, we formulate the Abel transform as a matrix $A \in \mathbb{R}^{m \times n}$ and the object radial density values as $\boldsymbol{\rho} \in \mathbb{R}^n$. Hence (1.1) is then discretized as

$$\mathbf{d} = A\boldsymbol{\rho}, \tag{1.2}$$

where $\mathbf{d} \in \mathbb{R}^m$. Here, m is a fixed number determined by the projection data projection. And n is independently chosed according to the discretization of $\boldsymbol{\rho}$. Usually, we set n is bigger than m.

In order to take into account the degradations occurring during the data production, we consider in what follows the general observation model given by

$$\mathbf{d} = KA\boldsymbol{\rho} + \mathbf{n}, \tag{1.3}$$

where $\mathbf{n}$ is a vector denoting the noise and K presents the blurring that may be produced in the process of radiographing.

In the literature, Hanson [14] has applied the Bayesian approaches to the tomographic reconstruction problem. Based on the work by Tikhonov in [25] and Rudin-Osher-Fatemi in [24], researchers have proposed a number of regularization methods [3, 4, 1, 2] for the Abel inversion. All these methods can be formulated as solving a minimization problem of the form:

$$\min_{\boldsymbol{\rho}} \left\{ \mu \mathcal{R}(\boldsymbol{\rho}) + \frac{1}{2} \|KA\rho - \mathbf{d}\|_2^2 \right\}, \tag{1.4}$$

where $\mathcal{R}(\boldsymbol{\rho})$ is a regularization functional based on Total-Variation (TV). Abraham *et al.* [1] has applied Chambolle's dual method [7] to solve the minimization problem in (1.4) for binary axial symmetric objects. In [4], the authors have proposed an adaptive TV method where the TV regularization is used to identify the locations of the suspected density discontinuities, and the H^1 regularization [4] acts on the data set apart from these locations. These existing methods focus on Abel inversion with noise removal for parallel X-ray beams and pay more attention to recover piecewise constant or at most linear density [4].

Unlike the pre-existing methods [3, 4, 2, 1], we focus on the tomographic reconstruction of 1D *piecewise smooth objects involving sharp edges*, radiographed by fan-beam X-rays. Our method is based on solving the regularized minimization problem of the form (1.4) where the regularization term $\mathcal{R}$ is designed to tackles the recovery of piecewise smooth objects involving edges. This constitutes the main novelty of our approach.

Since [21], using first-order TV gives rise to locally constant solutions while second-order TV as in [19] yields locally planar solutions without neat edges. So we focus on compound regularization $\mathcal{R}(\boldsymbol{\rho})$ mixing the ℓ_1 norms of the gradient and of the Laplacian of $\boldsymbol{\rho}$. A famous achievement in this direction being the TGV model of Bredies, Kunisch and Pock [6], we explored this regularization but results were not convincing. The best-suited compound regularization $\mathcal{R}(\boldsymbol{\rho})$ for our problem is much simpler: it is given by a linear combination of the ℓ_1 norms of the gradient and of the Laplacian of $\boldsymbol{\rho}$. According to the theory in [21], the corresponding solutions generically involve constant and linear shapes, as well as edges. The properties of high-order TV in keeping sharp edges and avoiding staircase effects on the smooth part have also been discussed in [8, 19, 20]. To solve the proposed high-order regularization problem, fast augmented Lagrangian method (ALM) is used. In addition, we shall also apply the proposed 1D technique for fan-beam X-rays to approximate 2D tomographic reconstruction for cone-beam X-rays. For the 2D problem, we treat the cone beam as a fan beam at parallel planes perpendicular to the symmetric axis. Then we apply the proposed algorithm on each layer to reconstruct the whole 2D cylindrical symmetric object. We compare our method

with several contemporary image restoration approaches. Extensive numerical tests confirm that our proposed high-order TV approach outperforms the concurrent methods in terms of restoration quality and computational costs. 2D numerical experiments show clearly the successful application of the proposed algorithm for 2D cylindrical object density reconstruction.

The rest of the paper is organized as follows: In §2, the discrete Abel transform for the fan-beam X-rays is described in more detail. In §3, we present the high-order TV regularized Abel inversion model and solve it with ALM. In §4, we introduce some other standard approaches that can be adapted to solve (1.4): (i) the TV model of [24]; (ii) the 4th-order model of [20]; and (iii) the total generalized variation model of [6]. In §5, we apply our algorithm to reconstruct piecewise smooth density functions for 1D axially symmetric and 2D cylindrically symmetric objects. Comparisons of our algorithm and other three standard approaches are also given in this section. We finally summarize and give some conclusions in §6.

2   Discrete Abel Transform for Fan-beam X-rays

First, we give some details on the discretization of the Abel transform. The projection matrix A is obtained by discretizing the Abel transform of equation (1.1). Here, we assume that the X-rays at different layers are parallel. Hence, the projection matrix A is always the same for each layer. In each layer, the projection matrix A is generated from fan-beam X-rays, as shown in Figure 1(b). We want to emphasis that this simplification has been used in industries.

Without loss of generality, we use the layer $z = 0$ to illustrate how to formulate the projection operator A, see Figure 1(b). Let $\rho(r)$ be the radial density for the layer. Since the object has finite volume, we can assume that $\rho(r) = 0$ when $r > R$. The distances from the source to the object and the object to the detector are denoted by L_1 and L_2 respectively, where $L_1 = |SO|$ and $L_2 = |OP_1|$. We consider Figure 1(b) on the rectangular coordinate system with origin O. Thus, the detector lies at plane $x = L_2$ and the areal density $d(y)$ is measured at $y \in [-H, H]$, where $H > (L1 + L2) \cdot R/L1$ to ensure that the projection data for the whole object is covered. Separate $[-H, H]$ into $2m - 1$ uniform partitions each with step size $\Delta_h = H/(m - 1)$. Considering the symmetry of the object, we only need half of the projection data. Take $\mathbf{d}$ to be a vector of m elements, with $d_i = d(y_i)$, for $i = 1, \cdots, m$. For the cross section of radius R, we subdivide $[0, R]$ into n uniform partitions with step size $\Delta_r = R/n$ and $r_i = i\Delta_r$. Then $\boldsymbol{\rho}$ is a vector of n elements with its i-th entry being $\rho(r_i)$. Hence, A is a matrix of size $m \times n$. The (i, j)-th element of A is equal to the length of the X-ray l_i lying between circles of $r = r_j$ and $r = r_{j+1}$.

The Abel projection operator A is very ill-conditioned, which makes the direct Abel inversion formula very sensitive to the noise contained in the measured data $\mathbf{d}$. To overcome the sensitivities, suitable regularization term $R(\boldsymbol{\rho})$ can be applied, as in (1.4).

3   Our Proposed Method—High-order TV Regularization

We propose the following minimization model to find the density function:

$$\min_{\boldsymbol{\rho}} \left\{ \mathcal{E}(\rho) = \mu_1 \|\nabla \boldsymbol{\rho}\|_1 + \mu_2 \|\Delta \boldsymbol{\rho}\|_1 + \frac{1}{2} \|KA\boldsymbol{\rho} - \mathbf{d}\|_2^2 \right\}, \tag{3.1}$$

where Δ is the discrete Laplacian operator, μ_1 and μ_2 are regularization constants that need to be properly chosen. In the next section, we shall introduce some standard regularization models in image processing. We shall modify these models to solve the Abel inversion problem and compare (3.1) against them.

It is common to use gradient descent method to solve the minimization problem (3.1). Recent research reveals that this kind of regularization problem can be solved much more efficiently using some special iterative procedures. Split-Bregman method [13] and augmented Lagrangian methods [28] have been experimentally proven to be some of the fastest methods in image processing.

As in [28, 26, 27], to apply the ALM to solve (3.1), we introduce two auxiliary variables $\mathbf{v}$ and $\mathbf{w}$ into (3.1) and reformulate the problem to be the following constrained minimization problem:

$$\min_{\boldsymbol{\rho},\mathbf{v},\mathbf{w}} \quad \left\{ \mu_1 \|\mathbf{v}\|_1 + \mu_2 \|\mathbf{w}\|_1 + \tfrac{1}{2}\|KA\boldsymbol{\rho} - \mathbf{d}\|_2^2 \right\} \tag{3.2}$$
$$\text{s. t.} \qquad \mathbf{v} = \nabla\boldsymbol{\rho}, \ \mathbf{w} = \Delta\boldsymbol{\rho}.$$

In order to solve the constrained minimization problem (3.2), we define the following augmented Lagrangian functional

$$
\begin{aligned}
\mathcal{L}(\boldsymbol{\rho},\mathbf{v},\mathbf{w};\mathbf{q}_1,\mathbf{q}_2) = \ & \mu_1\left(\|\mathbf{v}\|_1 + \langle \mathbf{q}_1, \mathbf{v} - \nabla\boldsymbol{\rho}\rangle + \frac{1}{2\gamma}\|\mathbf{v} - \nabla\boldsymbol{\rho}\|_2^2\right) \\
& + \mu_2\left(\|\mathbf{w}\|_1 + \langle \mathbf{q}_2, \mathbf{w} - \Delta\boldsymbol{\rho}\rangle + \frac{1}{2\eta}\|\mathbf{w} - \Delta\boldsymbol{\rho}\|_2^2\right) \\
& + \frac{1}{2}\|KA\boldsymbol{\rho} - \mathbf{d}\|_2^2,
\end{aligned}
\tag{3.3}
$$

with Lagrange multipliers $\mathbf{q}_1, \mathbf{q}_2$ and positive penalization constants γ, η. According to our tests, it is enough to take $\gamma = \eta = 1$.

It is known that one of the saddle points of the augmented Lagrangian functional corresponds to the minimizers of the constrained minimization problem (3.2) [28, 26, 27]. The following algorithm is often used to find the saddle points of augmented Lagrangian functionals:

Algorithm 1:

---

1. Initialize $\mathbf{v}^0 = \mathbf{0}, \mathbf{w}^0 = \mathbf{0}, \mathbf{q}_1^0 = \mathbf{0}, \mathbf{q}_2^0 = \mathbf{0}$;

2. For $k = 0, 1, 2, \cdots$:

   (a) Update $(\boldsymbol{\rho}^{k+1}, \mathbf{v}^{k+1}, \mathbf{w}^{k+1})$ by solving the following minimization problem with Lagrange multipliers $\mathbf{q}_1^k, \mathbf{q}_2^k$, i.e.

   $$(\boldsymbol{\rho}^{k+1}, \mathbf{v}^{k+1}, \mathbf{w}^{k+1}) = \arg\min_{\boldsymbol{\rho},\mathbf{v},\mathbf{w}} \mathcal{L}(\boldsymbol{\rho},\mathbf{v},\mathbf{w};\mathbf{q}_1^k,\mathbf{q}_2^k); \tag{3.4}$$

   (b) Update Lagrange multipliers $\mathbf{q}_1^{k+1}$ and $\mathbf{q}_2^{k+1}$ by

   $$\mathbf{q}_1^{k+1} = \mathbf{q}_1^k + \frac{1}{\gamma}(\mathbf{v}^{k+1} - \nabla\boldsymbol{\rho}^{k+1}), \quad \text{and} \quad \mathbf{q}_2^{k+1} = \mathbf{q}_2^k + \frac{1}{\eta}(\mathbf{w}^{k+1} - \Delta\boldsymbol{\rho}^{k+1}). \tag{3.5}$$

Since the variables in (3.4) is coupled together, it is very difficult to solve this minimization problem exactly. It is common to use an alternating minimization strategy to find approximate minimizers. In the following part, we separate problem (3.4) into three sub-problems and give details on how to apply an alternative minimization approach to find the approximate minimizers.

To find an approximate minimizer for (3.4), the following three sub-problems shall be solved sequentially once in each iteration.

- $\boldsymbol{\rho}$-subproblem: Given $\mathbf{v}, \mathbf{w}$,

$$\min_{\boldsymbol{\rho}} \left\{ \mu_1 \langle \mathbf{q}_1^k, -\nabla\boldsymbol{\rho} \rangle + \frac{\mu_1}{2\gamma} \|\mathbf{v} - \nabla\boldsymbol{\rho}\|_2^2 + \mu_2 \langle \mathbf{q}_2^k, -\Delta\boldsymbol{\rho} \rangle + \frac{\mu_2}{2\eta} \|\mathbf{w} - \Delta\boldsymbol{\rho}\|_2^2 + \frac{1}{2} \|KA\boldsymbol{\rho} - \mathbf{d}\|_2^2 \right\}. \quad (3.6)$$

- $\mathbf{v}$-subproblem: Given $\boldsymbol{\rho}, \mathbf{w}$,

$$\min_{\mathbf{v}} \left\{ \|\mathbf{v}\|_1 + \langle \mathbf{q}_1^k, \mathbf{v} - \nabla\boldsymbol{\rho} \rangle + \frac{1}{2\gamma} \|\mathbf{v} - \nabla\boldsymbol{\rho}\|_2^2 \right\}. \quad (3.7)$$

- $\mathbf{w}$-subproblem: Given $\boldsymbol{\rho}, \mathbf{v}$,

$$\min_{\mathbf{w}} \left\{ \|\mathbf{w}\|_1 + \langle \mathbf{q}_2^k, \mathbf{w} - \Delta\boldsymbol{\rho} \rangle + \frac{1}{2\eta} \|\mathbf{w} - \Delta\boldsymbol{\rho}\|_2^2 \right\}. \quad (3.8)$$

Next, we shall show that the three subproblems either have explicit solutions or can be solved by inexpensive numerical solvers.

3.1 Solving the ρ-subproblem

Notice that $\boldsymbol{\rho}$-sub problem is quadratic in $\boldsymbol{\rho}$. To find the solution of (3.6), we just need to take the derivative of its energy functional with respect to $\boldsymbol{\rho}$ and solve the following linear system

$$\mu_1 \text{div} \cdot \mathbf{q}_1^k + \frac{\mu_1}{\gamma} \text{div} \cdot (\mathbf{v} - \nabla\boldsymbol{\rho}) - \mu_2 \Delta \cdot \mathbf{q}_2^k + \frac{\mu_2}{\eta} \Delta \cdot (\Delta\boldsymbol{\rho} - \mathbf{w}) + A^\top K^\top (KA\boldsymbol{\rho} - \mathbf{d}) = 0, \quad (3.9)$$

where div denotes the divergence operator. In our simulations, this linear system is solved by a direct solver.

3.2 Solving the v-subproblem

Subproblem (3.7) is equivalent to

$$\min_{\mathbf{v}} \left\{ \gamma \|\mathbf{v}\|_1 + \frac{1}{2} \|\mathbf{v} - (\nabla\boldsymbol{\rho} - \gamma\mathbf{q}_1^k)\|_2^2 \right\}.$$

This subproblem has a closed-form solution which is given by the soft thresholding

$$\mathbf{v} = \mathcal{T}_\gamma(\nabla\boldsymbol{\rho} - \gamma\mathbf{q}_1^k), \quad (3.10)$$

where the i-th entry $v_i = \mathcal{T}_\gamma(\nabla_i\boldsymbol{\rho} - \gamma q_{1,i}^k)$ and $\mathcal{T}_\gamma$ is defined by

$$\mathcal{T}_\gamma(x) = \arg\min_y \{\gamma|y| + \frac{1}{2}|y - x|^2\} = \text{sign}(x)\max(|x| - \gamma, 0), \quad \text{for } x \in \mathbb{R}, \gamma > 0. \quad (3.11)$$

See [11].

3.3 Solving the w-subproblem

Similar to the **v**-subproblem, the **w**-subproblem is equivalent to

$$\min_{\mathbf{w}} \left\{ \eta \|\mathbf{w}\|_1 + \frac{1}{2} \|\mathbf{w} - (\Delta\boldsymbol{\rho} - \eta \mathbf{q}_2^k)\|_2^2 \right\}.$$

It has a closed-form solution given by

$$\mathbf{w} = \mathcal{T}_\eta(\Delta\boldsymbol{\rho} - \eta \mathbf{q}_2^k). \tag{3.12}$$

Combining the above results together, (3.4) is solved by the alternating minimization approach:

Algorithm 2: Alternating minimization approach for solving (3.4)

---

1. Initialize $\boldsymbol{\rho}^{k,0} = \boldsymbol{\rho}^k$, $\mathbf{v}^{k,0} = \mathbf{v}^k$, $\mathbf{w}^{k,0} = \mathbf{w}^0$;

2. For $l = 0, 1, 2, \cdots, L-1$:

   (a) Update $\boldsymbol{\rho}^{k,l+1}$ by solving (3.9), i.e.

$$\left(-\frac{\mu_1}{\gamma}\text{div} \cdot \nabla + \frac{\mu_2}{\eta}\Delta \cdot \Delta + A^\top K^\top K^\top A \right)\boldsymbol{\rho} = A^\top K^\top \mathbf{d} - \frac{\mu_1}{\gamma}\text{div} \cdot \left(\mathbf{v}^{k,l} + \gamma \mathbf{q}_1^k \right) + \frac{\mu_2}{\eta}\Delta \cdot \left(\mathbf{w}^{k,l} + \eta \mathbf{q}_2^k \right);$$

   (b) Update $\mathbf{v}^{k,l+1}$ using (3.10) for $\boldsymbol{\rho} = \boldsymbol{\rho}^{k,l+1}$;
   (c) Update $\mathbf{w}^{k,l+1}$ using (3.12) for $\boldsymbol{\rho} = \boldsymbol{\rho}^{k,l+1}$;

3. $\boldsymbol{\rho}^{k+1} = \boldsymbol{\rho}^{k,L}, \mathbf{v}^{k+1} = \mathbf{v}^{k,L}, \mathbf{w}^{k+1} = \mathbf{w}^{k,L}$.

We can see that the cost per iteration for the above scheme is very cheap. Numerical tests will also show that the total number of iterations needed to reach convergence is also very low.

4 Other Possible Regularization Techniques

In this section, we adapt several other popular contemporary methods in image restoration to solve Abel inversion problem (1.4). Augmented Lagrangian methods and corresponding schemes will also be derived for these regularization methods without going into much detail. In the numerical section, we will compare our model with these regularizers.

4.1 TV Regularization

The TV regularization model [24] has been successfully and widely applied to various problems in image processing. Its success relies on the remarkable ability of TV-norm in preserving edges and suppressing noise. The TV regularization methods for Abel inversion has been studied in [3, 4, 1, 2], Here we state the TV regularization method for the convenience of the comparison. We consider

$$\min_{\boldsymbol{\rho}} \left\{ \mu_1 \|\nabla\boldsymbol{\rho}\|_1 + \frac{1}{2} \|KA\boldsymbol{\rho} - \mathbf{d}\|_2^2 \right\}. \tag{4.1}$$

7

Many efficient methods have been proposed to solve (4.1) recently. For example, the very popular forward-backward splitting algorithm [10] combined with the Chambolle's TV denoising method [7], ALM [13, 28]. Here, we apply the ALM to solve (4.1). We introduce one auxiliary variable $\mathbf{v}$ into (4.1). Then (4.1) is equivalent to the following constrained minimization problem:

$$\min_{\boldsymbol{\rho},\mathbf{v}}\{\mu_1\|\mathbf{v}\|_1 + \frac{1}{2}\|KA\boldsymbol{\rho} - \mathbf{d}\|_2^2\} \quad \text{s.t. } \mathbf{v} = \nabla\boldsymbol{\rho}. \tag{4.2}$$

In order to solve (4.2), we define the following augmented Lagrangian functional

$$\mathcal{L}_1(\boldsymbol{\rho},\mathbf{v};\mathbf{q}_1) = \mu_1(\|\mathbf{v}\|_1 + \langle\mathbf{q}_1,\mathbf{v}-\nabla\boldsymbol{\rho}\rangle + \frac{1}{2\gamma}\|\mathbf{v}-\nabla\boldsymbol{\rho}\|_2^2) + \frac{1}{2}\|KA\boldsymbol{\rho}-\mathbf{d}\|_2^2, \tag{4.3}$$

with Lagrange multiplier $\mathbf{q}_1$ and positive constant γ. In our experiments, we always take $\gamma = 1$. The corresponding algorithm for finding the saddle point of this functional is the same algorithm by setting $\mu_2 = 0$ in Algorithm 1.

4.2 The LLT Model

In [19], Lysaker, Lundervold and Tai proposed a second-order method for image noise removal. For a given noisy image $\mathbf{u}_0$ in $\mathbb{R}^n$, the problem they considered is $\min_{\mathbf{u}}\left\{\mu_2\mathcal{R}(\mathbf{u}) + \frac{1}{2}\|\mathbf{u} - \mathbf{u}_0\|_2^2\right\}$, where

$$\mathcal{R}(\mathbf{u}) = \int\sqrt{\sum_{i,j=1}^{n}\left(\frac{\partial^2\mathbf{u}}{\partial\mathbf{x}_i\partial\mathbf{x}_j}\right)^2}d\mathbf{x} = \int|\mathcal{D}^2\mathbf{u}|dx, \quad \text{with} \quad \mathcal{D}^2\mathbf{u} = \left(\frac{\partial^2\mathbf{u}}{\partial\mathbf{x}_i\partial\mathbf{x}_j}\right)_{i,j=1}^{n}. \tag{4.4}$$

We apply the approach to the Abel inversion and consider

$$\min_{\boldsymbol{\rho}}\left\{\mu_2\mathcal{R}(\boldsymbol{\rho}) + \frac{1}{2}\|KA\boldsymbol{\rho} - \mathbf{d}\|_2^2\right\}. \tag{4.5}$$

In [26], ALM has been introduced for this kind of problems where an auxiliary variable is introduced into (4.5). In the discrete setting, the equivalent constrained problem is:

$$\min_{\boldsymbol{\rho},\mathbf{w}}\{\mu_2\|\mathbf{w}\| + \frac{1}{2}\|KA\boldsymbol{\rho} - \mathbf{d}\|_2^2\}, \text{ s.t. } \mathbf{w} = \mathcal{D}^2\boldsymbol{\rho} \tag{4.6}$$

where the differential operator $\mathcal{D}^2$ is to be replaced by its discrete counter part. We define the following augmented Lagrangian functional

$$\mathcal{L}_2(\boldsymbol{\rho},\mathbf{w};\mathbf{q}_2) = \mu_2(\|\mathbf{w}\|_1 + \langle\mathbf{q}_2,\mathbf{w}-\mathcal{D}^2\boldsymbol{\rho}\rangle + \frac{1}{2\eta}\|\mathbf{w}-\mathcal{D}^2\boldsymbol{\rho}\|_2^2) + \frac{1}{2}\|KA\boldsymbol{\rho}-\mathbf{d}\|_2^2, \tag{4.7}$$

where $\mathbf{q}_2$ is the Lagrange multiplier and η is a positive parameter which is always taken to be 1 in all our tests. For 1D problems, we have $\mathcal{D}^2 = \Delta$, the discrete Laplacian, and the corresponding algorithm for finding the saddle point of (4.7) is then an algorithm by setting $\mu_1 = 0$ in Algorithm 1.

4.3 TGV Regularization

Total generalized variation (TGV) was proposed in [6] and is defined by

$$\text{TGV}_\nu^k(\mathbf{u}) = \sup\left\{\int_\Omega\mathbf{u}\,\text{div}^k\mathbf{v}d\mathbf{x} \mid \mathbf{v}\in\mathcal{C}_c^k(\Omega,\text{Sym}^k(\mathbb{R}^d)), \|\text{div}_\infty^l\mathbf{v}\| \leq \nu_l,\ l=0,\cdots,k-1\right\}. \tag{4.8}$$

Here $\text{Sym}^k(\mathbb{R}^d)$ denotes the space of symmetric tensors of order k, $\mathcal{C}_c^k(\Omega, \text{Sym}^k(\mathbb{R}^d)) = \{\xi \in \mathcal{C}^k(\bar{\Omega}, \text{Sym}^k(\mathbb{R}^d)) \mid \text{supp } \xi \subset\subset \Omega\}$, and $\nu = (\nu_0, \nu_1, \cdots, \nu_{k-1})$ is a fixed positive parameter set. If $k = 1, \nu_0 = 1$, TGV_ν^k coincides with TV. As $k > 1$, TGV_ν^k involves higher order derivatives, which is referred as total generalized bounded variation semi-norm. Comparing with TV, the high-order TGV has a novel property in avoiding the staircasing effect for reconstructing the affine and even smooth images. In [6], the authors solved

$$\min_{\mathbf{u}} \left\{ \text{TGV}_\nu^2(\mathbf{u}) + \frac{1}{2}\|\mathbf{u} - \mathbf{u}_0\|_2^2 \right\}. \tag{4.9}$$

as an example to illustrate the high quality of TGV in image denoising. There, primal-dual algorithm is developed to solve (4.9) and the idea is later adopted to solve an MRI reconstruction problem in [17].

To introduce the dual algorithm, we begin from the dual form of the total variation

$$\text{TV}(\mathbf{u}) = \sup_{\mathbf{v}} \left\{ \int_\Omega \mathbf{u} \text{ div } \mathbf{v} d\mathbf{x} \mid \mathbf{v} \in \mathcal{C}_c^1(\Omega, \mathbb{C}^n), \ \|\mathbf{v}\|_\infty \leq 1 \right\}, \tag{4.10}$$

whose supremum is attained at $\mathbf{v} = -\nabla\mathbf{u}/|\nabla\mathbf{u}|$. This is the special case of (4.8) with $\nu_0 = 1$ and $k = 1$. When $k = 2$, TGV_ν^2 can be represented as

$$\text{TGV}_\nu^2(\mathbf{u}) = \min_{\mathbf{v}} \left\{ \nu_1 \int_\Omega |\nabla\mathbf{u} - \mathbf{v}| \ d\mathbf{x} + \nu_0 \int_\Omega |E(\mathbf{v})| \ d\mathbf{x} \right\}, \tag{4.11}$$

where $E(\mathbf{v}) = \frac{1}{2}(\nabla\mathbf{v} + \nabla\mathbf{v}^\top)$ denotes the symmetrized derivative [6, 17].

Here we adopt the same primal-dual approach to solve the TGV regularized Abel inversion:

$$\min_{\boldsymbol{\rho}} \left\{ \text{TGV}_\nu^2(\boldsymbol{\rho}) + \frac{1}{2}\|KA\boldsymbol{\rho} - \mathbf{b}\|_2^2 \right\}. \tag{4.12}$$

Introducing (4.11) into (4.12), then minimization problem (4.12) becomes

$$\min_{\boldsymbol{\rho},\mathbf{v}} \left\{ \nu_1\|\nabla\boldsymbol{\rho} - \mathbf{v}\|_1 + \nu_0\|E(\mathbf{v})\|_1 + \frac{1}{2}\|KA\boldsymbol{\rho} - \mathbf{b}\|_2^2 \right\}. \tag{4.13}$$

Minimization problem (4.13) is then solved by a convex-concave saddle-point approach based on the duality principles:

$$\min_{\boldsymbol{\rho},\mathbf{v}} \max_{\mathbf{p}\in P, \mathbf{q}\in Q, \mathbf{r}\in\mathbb{R}^n} \left\{ \langle\nabla\boldsymbol{\rho} - \mathbf{v}, \mathbf{p}\rangle + \langle E(\mathbf{v}), \mathbf{q}\rangle + \langle KA\boldsymbol{\rho} - \mathbf{b}, \mathbf{r}\rangle - \frac{1}{2}\|\mathbf{r}\|_2^2 \right\}, \tag{4.14}$$

where $P = \{\mathbf{p} \in \mathbb{R}^n \mid \|\mathbf{p}\|_\infty \leq \nu_1\}$, $Q = \{\mathbf{q} \in \mathbb{R}^n \mid \|\mathbf{q}\|_\infty \leq \nu_0\}$, and $\mathbf{r} \in \mathbb{R}^n$ is the dual variable with respect to the data-fitting term. We denote the Euclidean projectors onto the convex sets P, Q by $\text{proj}_P(\tilde{\mathbf{p}})$, $\text{proj}_Q(\tilde{\mathbf{q}})$ respectively. The projections can be easily computed by pointwise operations:

$$\text{proj}_P(\tilde{\mathbf{p}}) = \frac{\tilde{\mathbf{p}}}{\max(1, \frac{|\tilde{\mathbf{p}}|}{\nu_1})}, \quad \text{proj}_Q(\tilde{\mathbf{q}}) = \frac{\tilde{\mathbf{q}}}{\max(1, \frac{|\tilde{\mathbf{q}}|}{\nu_0})} \ .$$

In addition, we denote

$$\text{proj}_2^\sigma(\tilde{\mathbf{r}}) = \arg\min_{\mathbf{r}\in\mathbb{R}^n} \left\{ \frac{\|\mathbf{r} - \tilde{\mathbf{r}}\|_2^2}{2\sigma} + \frac{1}{2}\|\mathbf{r}\|_2^2 \right\} = \frac{\tilde{\mathbf{r}}}{1 + \sigma}.$$

The following primal-dual algorithm will be used for solving the TGV regularized Abel inversion (4.14). For more details on the derivation and analysis of this algorithm, the interested readers can refer to [6]:

Algorithm 3:

---

1. Initialize $\boldsymbol{\rho}^0, \hat{\boldsymbol{\rho}} = 0, \mathbf{v}^0, \hat{\mathbf{v}}^0 = 0, \mathbf{p}^0 = 0, \mathbf{q}^0 = 0, \mathbf{r}^0 = 0$, choose step size τ, σ;

2. **Repeat until** $\{\boldsymbol{\rho}^k\}$ converges:
   $\mathbf{p}^{k+1} = \mathrm{proj}_P(\mathbf{p}^k + \sigma(\nabla \hat{\boldsymbol{\rho}}^k - \hat{\mathbf{v}}^k))$;
   $\mathbf{q}^{k+1} = \mathrm{proj}_Q(\mathbf{q}^k + \sigma E(\hat{\mathbf{v}}^k))$;
   $\mathbf{r}^{k+1} = \mathrm{prox}_2^\sigma(\mathbf{r}^k + \sigma(KA\hat{\rho}^k - \mathbf{b}))$;
   $\boldsymbol{\rho}_{\mathrm{old}}^{k+1} = \boldsymbol{\rho}^k$;
   $\boldsymbol{\rho}^{k+1} = \boldsymbol{\rho}^k + \tau(\mathrm{div}_1 \mathbf{p}^{k+1} - A^\top K^\top \mathbf{r}^{k+1})$;
   $\hat{\boldsymbol{\rho}}^{k+1} = 2\boldsymbol{\rho}^{k+1} - \boldsymbol{\rho}_{\mathrm{old}}^{k+1}$;
   $\mathbf{v}_{\mathrm{old}}^{k+1} = \mathbf{v}^k$;
   $\mathbf{v}^{k+1} = \mathbf{v}^k + \tau(\mathbf{p}^{k+1} + \mathrm{div}_2 \mathbf{q}^{k+1})$;
   $\hat{\mathbf{v}}^{k+1} = 2\mathbf{v}^{k+1} - \mathbf{v}_{\mathrm{old}}^{k+1}$;

---

where div_1 is divergence operator of ∇ and div_2 is divergence operator of E. The convergence of the algorithm is guaranteed provided that $\sigma\tau < (9 + \sqrt{8})^{-1}$. In our experiment, we take $\sigma = \tau = 1/16$.

5 Numerical Results

In this section, we apply all the compared methods to tomography reconstruction. We will also use the 1D techniques to the 2D problems. The regularization parameters $\mu, \mu_1, \mu_2, \nu_0, \nu_1$ are chosen by trial and error. Their values are given in the subfigures of Figure $2 - 7$.

5.1 Numerical tests in 1D

In this section, we show the numerical results of the proposed algorithm on the tomography reconstruction for some 1D objects.

To simulate the possible phenomenon which could happen in real applications, we construct two objects with function $\rho(r)$ consisting of constant, linear and curve parts. See Figures 2 and 5. In the first three tests, the blur is not considered. In these examples, R, L_1, L_2 of Figure 1(b) are taken to be 5cm, 349cm and 449cm respectively. From the numerical tests, we find that 280 partitions for the radius r and 512 measuring points for $\mathbf{d}$ are enough. More partitions increase more computational cost, but no much improvement for the reconstructions. See Figure 4 of 560 partitions for comparition. Taking 280 partitions, $\boldsymbol{\rho}$ is a vector of $n = 280$ elements and $\mathbf{d}$ of $m = 256$ elements. Figures 2 and 3 show the reconstruction results for different noise levels for the first example. Figure 5 shows the reconstruction result for the second example. Inspecting the recovered results and the computational costs produced by TV, LLT, TGV, and high-order TV regularization methods, the high-order TV is the most competitive.

In Figure 2, we take the noise variance to be 1% of the maximum noiseless projection data. In Figure 3, we take the noise variance to be 1.5%. The reconstruction results are shown in Figure 2(c)–2(f), and Figure 3(c)–3(f) respectively. Figure 2(c) and 3(c) show that TV regularization based reconstruction is severely affected by the "staircase" effect at the linear and curvilinear parts, while

the high-order TV regularization model can reduce the staircase effect, meanwhile preserves the edges and the density level, *cf.* Figure 2(d)–2(f) and 3(d)–3(f).

The density function in Figure 4 is the same to that in Figure 2 and 3 but with 560 partitions for radius and 1024 measuring points for **d**. Therefore, in this example, $\boldsymbol{\rho}$ is a vector of $n = 560$ elements and **d** of $m = 512$ elements. The noise variance here is taken to be 1.5% of the maximum noiseless projection data.

Figure 5 shows the reconstruction results on another piecewise smooth density function. Here, we take the noise variance to be 1.5% of the maximum noiseless projection data. The reconstruction results are shown in Figure 5(c)–5(f). As in Figures 2 and 3, the high-order TV regularization method is the most competitive among all the compared methods, *cf.* Figure 5(f).

Next, we consider the density reconstruction from the blurred and noisy areal density. The blurring matrix K is generated by the MATLAB command: `fspecial('Gaussian', [7,1], 1)`. The reconstruction results are shown in Figure 6.

From Figure 2 – 6, we can have an "eyeball" impression of the reconstruction quality by different methods. The reconstructions by the TV regularized model are polluted by "staircases", while LLT, TGV and high-order TV models reduce the staircase phenomenon and meanwhile keeps the sharp edges. To show the quantitative comparison, we list the signal-to-noise ratio (SNR) in Table 1. SNR has been used in [27], which is defined by

$$\text{SNR} =: 10 \log_{10} \frac{\|\mathbf{u} - M(\mathbf{u})\|_2^2}{\|\hat{\mathbf{u}} - \mathbf{u}\|_2^2} (\mathbf{dB}).$$

Here **u** and $\hat{\mathbf{u}}$ denote the original signal and the restored signal respectively, and $M(\mathbf{u})$ is the mean gray-level value of the original signal. The largest SNR values are in italic. Amongst all the results, the high-order TV produces the largest SNR values.

To see the details of the density reconstruction, we show several slices of the recovered functions by different algorithms. In Figure 8, left column is for layer 256, which corresponds to the cross section $z = 0$. Middle column is for layer 200, and right column for layer 100. From Figure 8, we see that reconstruction by high-order TV shows the best restoration in view of the edge reservation and density value accuracy. The 2D image restoration is evaluated by its SNR value. We have compared the SNR values in Table 1.

Figure	TV	LLT	TGV	High-order TV
2	20.4211	23.5092	23.5245	*25.0431*
3	19.3409	20.8442	20.6134	*23.8263*
4	19.5428	22.8945	22.2193	*23.9042*
5	18.3551	19.5241	19.5255	*21.8096*
6	19.7328	17.2194	20.3809	*21.5414*
7	22.5398	22.5345	22.3205	*22.9822*

Table 1: Comparisons of SNR of the reconstruction results by TV, LLT, TGV, and high-order TV regularization (our method) methods for examples shown in Figures 2–7. The largest SNR values are in italic.

5.2 Numerical tests in 2D

In this section, we apply the TV, LLT, TGV, and high-order TV regularizers to the tomographic reconstruction for general cylindrically symmetric objects (2D) from a single radiograph. The
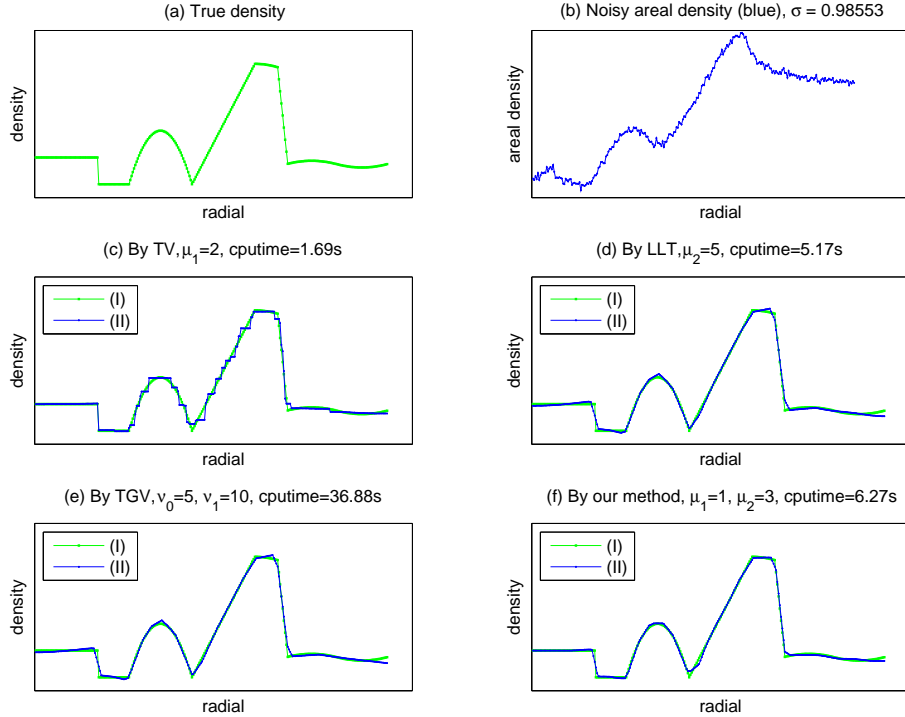
Figure 2: Abel inversion for piecewise smooth object. The object density is defined at 280 radial positions and composed of piecewise smooth and piecewise constant functions. The areal density is corrupted with Gaussian noise at level 1% of maximum of the noiseless projection data, shown in (b). In subfigures (c)–(f), green line presents true density, while blue presents the recovered density. The reconstruction by TV is staircase in linear and curvilinear part. Other methods provide acceptable reconstructions, as shown in (d)–(f). Among them, our method (high-order TV regularizer) (f) is the most competitive considering reconstruction effect and computational cost.

radiograph is taken by cone-beam X-rays. To do tomographic reconstruction, we approximate the cone-beam by fan-beam lying in different parallel planes perpendicular to the symmetry axis of the object. As discussed in Section 1, each object layer is recovered by solving our proposed model, and it is a 1D tomography problem. The whole density is reconstructed layer by layer. Here, we use the same projection operator A (at layer $z = 0$) to reconstruct the density function for all the layers.

We simulate a spherical object. Its density profile passing through the symmetric axis is shown in Figure 7(a), which is a piecewise smooth function of radius r. The radiograph of the object is 7(b) which is an image is of size 512×512. It is contaminated by Gaussian noise. The noise variance is taken to be 1.5% of the maximum of noiseless projection data for each layer. In the process of density reconstruction, the regularization parameters are identical in different layers, which have been listed in Figure 7. Figure 7(c)–7(f) show the reconstruction results by TV, LLT, TGV, and high-order TV models. The SNR values of the reconstructions have been listed in Table 1. We see that the high-order TV regularizers reaches the highest SNR value.
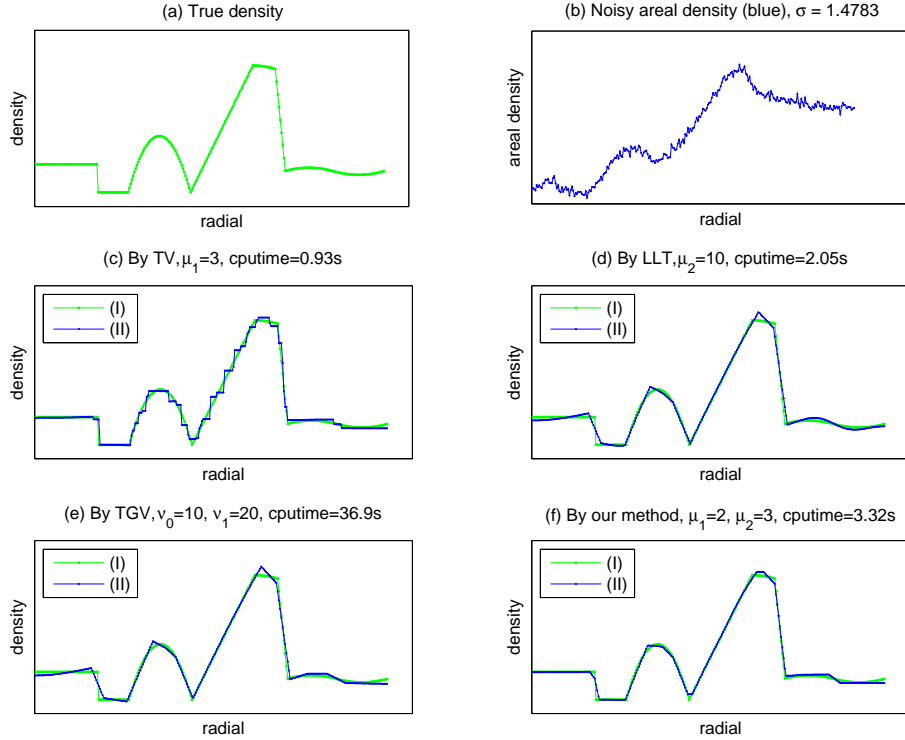
Figure 3: Abel inversion for different noise level. The object density is defined at 280 radial positions. It is the same function as in Figure 2. The areal density is corrupted with Gaussian noise at level 1.5% of maximum of the noiseless projection data. From subfigures (c)–(f), green line corresponds to true density, while blue the recovered density, we give different reconstructions by TV, LLT, TGV and our model. For high noise level, our method keeps the most competitive resconstruction.

To see the details of the density reconstruction, we show several slices of the recovered functions by different algorithms. In Figure 8, left column is for layer 256, which corresponds to the cross section $z = 0$. Middle column is for layer 200, and right column for layer 100. From Figure 8, we see that reconstruction by high-order TV shows the best restoration in view of the edge reservation and density value accuracy. The 2D image restoration is evaluated by its SNR value. We have compared the SNR values in Table 1.

6   Conclusion

In this paper, we concentrate on the tomographic reconstruction technique for axially symmetric objects from a single radiograph formed by fan-beam X-rays. To deal with the ill-posedness of Abel inversion, we apply the high-order TV regularization method based on its good property in reducing staircase effect and meanwhile keeping sharp edges. Fast ALM is applied to solve the high-order TV regularization model. We compare three other models in terms of CPU time costs, SNR values as well as feature reconstruction. Numerical results show that high-order TV improves well density
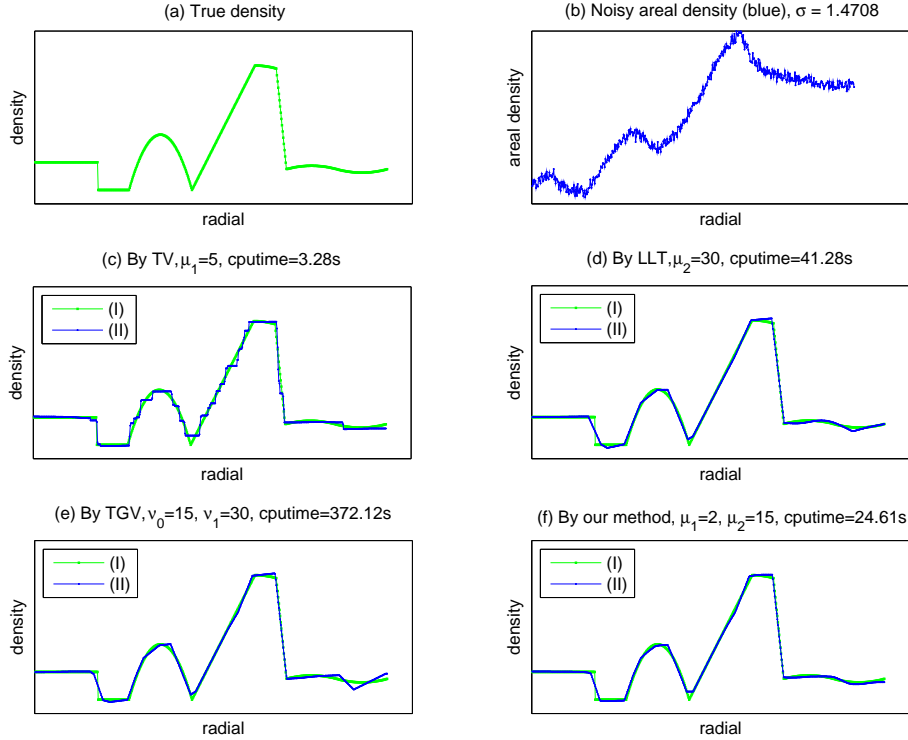
Figure 4: Abel inversion by using more projection data. For the same object of Figure 3, we divide the object radius by 560 partitions. The areal density is recorded at 512 points. It is corrupted by Gaussian noise at level 1.5% of maximum of the noiseless projection data. Similar to Figures 2 and 3, in subfigures (c)–(f), green is the true value and blue is the recovered, we see that the reconstruction quality is improved a little by using more projection points and subdividing radius. Meanwhile, the computational cost increases a lot.

level preservation comparing to the other potentially good methods. To recover any cylindrical symmetric object (2D) radiographed by a cone beam X-rays, the high-order TV regularization method is applied layer by layer. Numerical results show that our method is efficient for 2D object tomographic reconstruction.

APPENDIX

In this appendix, we adapt the convergence theory in [27] to prove the convergence of Algorithm 1 with $L \to \infty$ and $L = 1$ in Algorithm 2 respectively. Based on the theory in convex analysis [15], problem (3.1) has minimizers, and especially has a unique minimizer if KA is column full-rank. In addition, we have a similar result as Theorem 4.1 in [27].

Proposition $\boldsymbol{\rho}^*$ *is a solution of (3.1), if and only if there exists* $(\boldsymbol{\rho}^*, \mathbf{v}^*, \mathbf{w}^*; \mathbf{q}_1^*, \mathbf{q}_2^*)$ *being a saddle point of (3.2).*

The proof can be easily obtained referring from Theorem 4.1 of [27]. In this section, we mainly
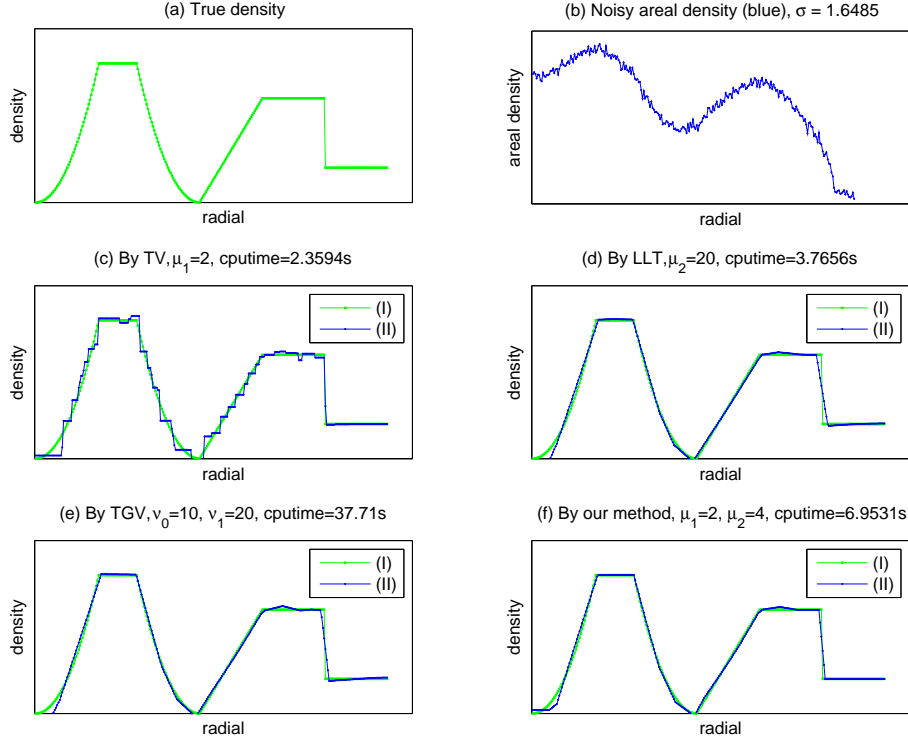
Figure 5: Abel inversion for different object. The object density is defined at 280 radial positions and mixed by piecewise smooth and piecewise constant functions. The areal density is corrupted with Gaussian noise at level 1.5% of maximum of the noiseless projection data. From subfigures (c)–(f), we show different reconstructions by TV, LLT, TGV and our model. We get the same impression that our proposed model is the most efficient.

adapts the proof for Theorem 4.2 and Theorem 4.3 in [27] to discuss the convergence of Algorithm 1 with $L \to \infty$ and $L = 1$.

Theorem 1 *Assume $(\boldsymbol{\rho}^*, \mathbf{v}^*, \mathbf{w}^*; \mathbf{q}_1^*, \mathbf{q}_2^*)$ be a saddle-point of $\mathcal{L}(\boldsymbol{\rho}, \mathbf{v}, \mathbf{w}; \mathbf{q}_1, \mathbf{q}_2)$. Suppose that the minimization problem (3.4) is exactly solved in each iteration, i.e. $L \to \infty$ in Algorithm 2. Then the sequence $(\boldsymbol{\rho}^k, \mathbf{v}^k, \mathbf{w}^k; \mathbf{q}_1^k, \mathbf{q}_2^k)$ satisfies*

$$
\begin{cases}
\lim_{k \to \infty} \mu_1 \|\mathbf{v}^k\|_1 + \mu_2 \|\mathbf{w}^k\|_1 + \frac{1}{2}\|KA\boldsymbol{\rho}^k - \mathbf{d}\|_2^2 = \mathcal{E}(\boldsymbol{\rho}^*), \\
\lim_{k \to \infty} \|\mathbf{v}^k - \nabla\boldsymbol{\rho}^k\|_2 = 0, \\
\lim_{k \to \infty} \|\mathbf{w}^k - \Delta\boldsymbol{\rho}^k\|_2 = 0, \\
\lim_{k \to \infty} \|KA(\boldsymbol{\rho}^k - \boldsymbol{\rho}^*)\|_2 = 0.
\end{cases}
\tag{6.1}
$$

Moreover, (6.1) indicates that $\{\boldsymbol{\rho}^k\}$ is a minimizing sequence of $\mathcal{E}(\cdot)$. If the minimizer of $\mathcal{E}(\cdot)$ is unique , then $\boldsymbol{\rho}^k \to \boldsymbol{\rho}^*$.

Proof: Let us define $\bar{\boldsymbol{\rho}}^k, \bar{\mathbf{v}}^k, \bar{\mathbf{w}}^k, \bar{\mathbf{q}}_1^k, \bar{\mathbf{q}}_2^k$ as

$$
\bar{\boldsymbol{\rho}}^k = \boldsymbol{\rho}^k - \boldsymbol{\rho}^*, \bar{\mathbf{v}}^k = \mathbf{v}^k - \mathbf{v}^*, \bar{\mathbf{w}}^k = \mathbf{w}^k - \mathbf{w}^*, \bar{\mathbf{q}}_1^k = \mathbf{q}_1^k - \mathbf{q}_1^*, \bar{\mathbf{q}}_2^k = \mathbf{q}_2^k - \mathbf{q}_2^*.
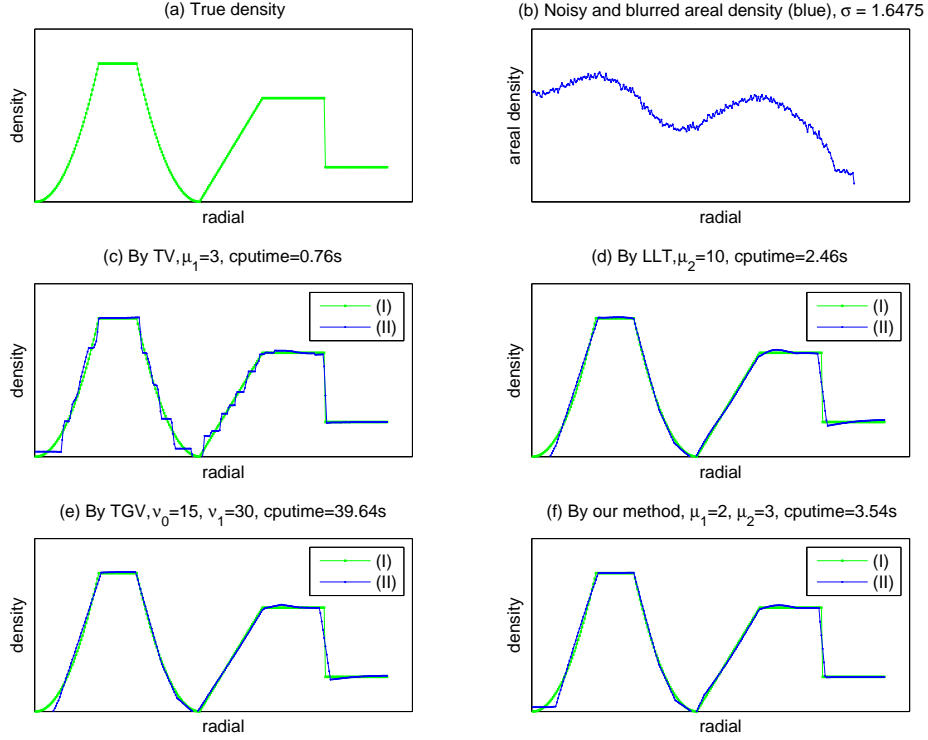$$

Figure 6: Abel inversion for noisy and blurred projection data. The object density is defined at 280 radial positions. The areal density is corrupted by Gaussian noise and blur. The blur is generated by the MATLAB command: `fspecial('Gaussian', [7,1], 1)`. The noise level is 1.5% of maximum of the noiseless blurred projection data. By subfigures (c)–(f), we show density reconstructions by different methods from noisy and blurred data. Our method is efficient to recover density from the noisy and blurred projection data.

Since $(\boldsymbol{\rho}^*, \mathbf{v}^*, \mathbf{w}^*; \mathbf{q}_1^*, \mathbf{q}_2^*)$ is a saddle-point of $\mathcal{L}(\boldsymbol{\rho}, \mathbf{v}, \mathbf{w}; \mathbf{q}_1, \mathbf{q}_2)$, we have

$$\mathcal{L}(\boldsymbol{\rho}^*, \mathbf{v}^*, \mathbf{w}^*; \mathbf{q}_1, \mathbf{q}_2) \leq \mathcal{L}(\boldsymbol{\rho}^*, \mathbf{v}^*, \mathbf{w}^*; \mathbf{q}_1^*, \mathbf{q}_2^*) \leq \mathcal{L}(\boldsymbol{\rho}, \mathbf{v}, \mathbf{w}; \mathbf{q}_1^*, \mathbf{q}_2^*), \tag{6.2}$$

and

$$\begin{cases} \mathbf{v}^* = \nabla \boldsymbol{\rho}^* \\ \mathbf{w}^* = \Delta \boldsymbol{\rho}^*. \end{cases} \tag{6.3}$$

This relationship, together with (3.5), indicates

$$\begin{cases} \bar{\mathbf{q}}_1^{k+1} = \bar{\mathbf{q}}_1^k + \frac{1}{\gamma}(\bar{\mathbf{v}}^{k+1} - \nabla \bar{\boldsymbol{\rho}}^{k+1}) \\ \bar{\mathbf{q}}_2^{k+1} = \bar{\mathbf{q}}_2^k + \frac{1}{\eta}(\bar{\mathbf{w}}^{k+1} - \Delta \bar{\boldsymbol{\rho}}^{k+1}) \end{cases},$$

which is equivalent to

$$\begin{cases} \sqrt{\frac{1}{\eta}}\bar{\mathbf{q}}_1^{k+1} = \sqrt{\frac{1}{\eta}}\bar{\mathbf{q}}_1^k + \frac{1}{\gamma}\sqrt{\frac{1}{\eta}}(\bar{\mathbf{v}}^{k+1} - \nabla \bar{\boldsymbol{\rho}}^{k+1}) \\ \sqrt{\frac{1}{\gamma}}\bar{\mathbf{q}}_2^{k+1} = \sqrt{\frac{1}{\gamma}}\bar{\mathbf{q}}_2^k + \frac{1}{\eta}\sqrt{\frac{1}{\gamma}}(\bar{\mathbf{w}}^{k+1} - \Delta \bar{\boldsymbol{\rho}}^{k+1}) \end{cases}.$$
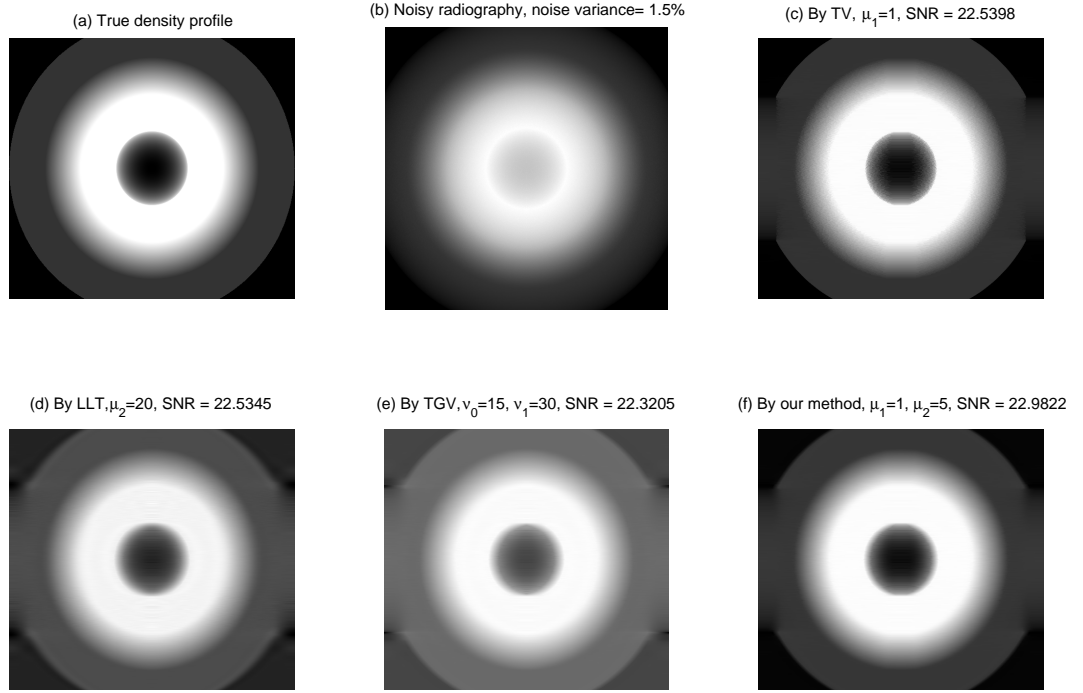
16

(a) True density profile

(b) Noisy radiography, noise variance= 1.5%

(c) By TV, μ_1=1, SNR = 22.5398

(d) By LLT,μ_2=20, SNR = 22.5345

(e) By TGV,v_0=15, v_1=30, SNR = 22.3205

(f) By our method, μ_1=1, μ_2=5, SNR = 22.9822

Figure 7: 2D tomographic reconstructions.

It follows that

$$
\left(\frac{\mu_1}{\eta} \| \bar{\mathbf{q}}_1^k \|_2^2 + \frac{\mu_2}{\gamma} \| \bar{\mathbf{q}}_2^k \|_2^2 \right) - \left(\frac{\mu_1}{\eta} \| \bar{\mathbf{q}}_1^{k+1} \|_2^2 + \frac{\mu_2}{\gamma} \| \bar{\mathbf{q}}_2^{k+1} \|_2^2 \right)
$$

$$
= -\frac{2\mu_1}{\eta\gamma} \langle \bar{\mathbf{q}}_1^k, \bar{\mathbf{v}}^{k+1} - \nabla \bar{\boldsymbol{\rho}}^{k+1} \rangle - \frac{\mu_1}{\eta\gamma^2} \| \bar{\mathbf{v}}^{k+1} - \nabla \bar{\boldsymbol{\rho}}^{k+1} \|_2^2 - \frac{2\mu_2}{\eta\gamma} \langle \bar{\mathbf{q}}_2^k, \bar{\mathbf{w}}^{k+1} - \Delta \bar{\boldsymbol{\rho}}^{k+1} \rangle \quad (6.4)
$$

$$
- \frac{\mu_2}{\eta^2\gamma} \| \bar{\mathbf{w}}^{k+1} - \Delta \bar{\boldsymbol{\rho}}^{k+1} \|_2^2.
$$

In the following, we show that the right hand side of (6.4) is no less than 0 and thus the sequence $\left\{ \left(\frac{\mu_1}{\eta} \| \bar{\mathbf{q}}_1^k \|_2^2 + \frac{\mu_2}{\gamma} \| \bar{\mathbf{q}}_2^k \|_2^2 \right) \right\}$ is monotonically decreasing. From the inequality of (6.2), $(\boldsymbol{\rho}^*, \mathbf{v}^*, \mathbf{w}^*)$ is characterized by

$$
\mu_1 \langle \mathrm{div} \cdot \mathbf{q}_1^*, \boldsymbol{\rho} - \boldsymbol{\rho}^* \rangle - \frac{\mu_1}{\gamma} \langle \mathrm{div} \cdot (\nabla \boldsymbol{\rho}^* - \mathbf{v}^*), \boldsymbol{\rho} - \boldsymbol{\rho}^* \rangle - \mu_2 \langle \Delta \cdot \mathbf{q}_2^*, \boldsymbol{\rho} - \boldsymbol{\rho}^* \rangle
$$

$$
+ \frac{\mu_2}{\eta} \langle \Delta \cdot (\Delta \boldsymbol{\rho}^* - \mathbf{w}^*), \boldsymbol{\rho} - \boldsymbol{\rho}^* \rangle + \langle A^\top K^\top (KA\boldsymbol{\rho}^* - \mathbf{d}, \boldsymbol{\rho} - \boldsymbol{\rho}^*) \rangle \geq 0, \quad (6.5)
$$

$$
\| \mathbf{v} \|_1 - \| \mathbf{v}^* \|_1 + \langle \mathbf{q}_1^*, \mathbf{v} - \mathbf{v}^* \rangle + \frac{1}{\gamma} \langle \mathbf{v}^* - \nabla \boldsymbol{\rho}^*, \mathbf{v} - \mathbf{v}^* \rangle \geq 0, \quad (6.6)
$$

$$
\| \mathbf{w} \|_1 - \| \mathbf{w}^* \|_1 + \langle \mathbf{q}_2^*, \mathbf{w} - \mathbf{w}^* \rangle + \frac{1}{\eta} \langle \mathbf{w}^* - \Delta \boldsymbol{\rho}^*, \mathbf{w} - \mathbf{w}^* \rangle \geq 0. \quad (6.7)
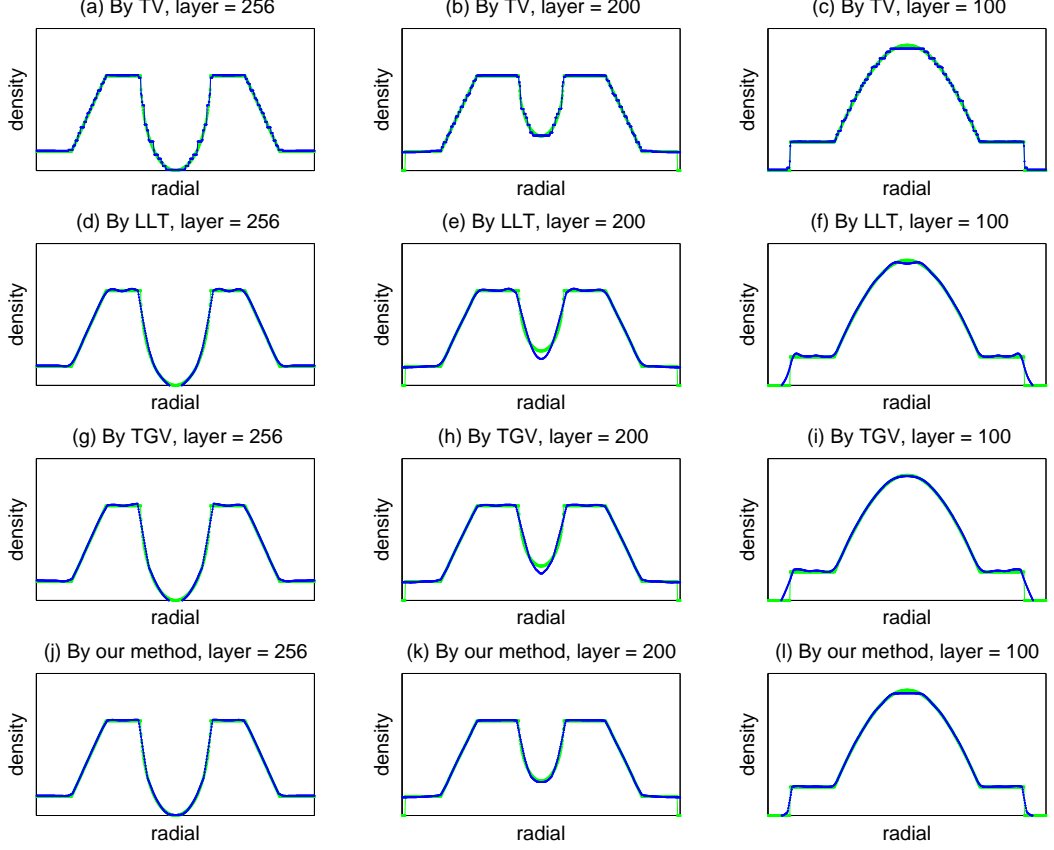$$

17

Figure 8: 2D tomographic reconstruction for layer 256, 200, 100. Left column is for layer 256; middle column is for layer 200, and right column is for layer 100.

Similarly, $(\boldsymbol{\rho}^{k+1}, \mathbf{v}^{k+1}, \mathbf{w}^{k+1})$ is characterized by

$$\mu_1 \langle \text{div} \cdot \mathbf{q}_1^k, \boldsymbol{\rho} - \boldsymbol{\rho}^{k+1} \rangle - \frac{\mu_1}{\gamma} \langle \text{div} \cdot (\nabla \boldsymbol{\rho}^{k+1} - \mathbf{v}^{k+1}), \boldsymbol{\rho} - \boldsymbol{\rho}^{k+1} \rangle - \mu_2 \langle \Delta \cdot \mathbf{q}_2^k, \boldsymbol{\rho} - \boldsymbol{\rho}^{k+1} \rangle$$

$$+ \frac{\mu_2}{\eta} \langle \Delta \cdot (\Delta \boldsymbol{\rho}^{k+1} - \mathbf{w}^{k+1}), \boldsymbol{\rho} - \boldsymbol{\rho}^{k+1} \rangle + \langle A^\top K^\top (KA\boldsymbol{\rho}^{k+1} - \mathbf{d}, \boldsymbol{\rho} - \boldsymbol{\rho}^{k+1}) \rangle \geq 0, \qquad (6.8)$$

$$\|\mathbf{v}\|_1 - \|\mathbf{v}^{k+1}\|_1 + \langle \mathbf{q}_1^k, \mathbf{v} - \mathbf{v}^{k+1} \rangle + \frac{1}{\gamma} \langle \mathbf{v}^{k+1} - \nabla \boldsymbol{\rho}^{k+1}, \mathbf{v} - \mathbf{v}^{k+1} \rangle \geq 0, \qquad (6.9)$$

$$\|\mathbf{w}\|_1 - \|\mathbf{w}^{k+1}\|_1 + \langle \mathbf{q}_2^k, \mathbf{w} - \mathbf{w}^{k+1} \rangle + \frac{1}{\eta} \langle \mathbf{w}^{k+1} - \Delta \boldsymbol{\rho}^{k+1}, \mathbf{w} - \mathbf{w}^{k+1} \rangle \geq 0, \qquad (6.10)$$

since $(\boldsymbol{\rho}^{k+1}, \mathbf{v}^{k+1}, \mathbf{w}^{k+1})$ is the solution of (3.4). Take $\boldsymbol{\rho} = \boldsymbol{\rho}^{k+1}$ in (6.5), $\boldsymbol{\rho} = \boldsymbol{\rho}^*$ in (6.8), $\mathbf{v} = \mathbf{v}^{k+1}$ in (6.6), $\mathbf{v} = \mathbf{v}^*$ in (6.9), $\mathbf{w} = \mathbf{w}^{k+1}$ in (6.7), and $\mathbf{w} = \mathbf{w}^*$ in (6.10), respectively. Taking addition (6.5)+(6.8)+μ_1[(6.6)+(6.9)]+μ_2[(6.7)+(6.10)], we have

$$-\mu_1 \langle \mathbf{q}_1^k, \bar{\mathbf{v}}^{k+1} - \nabla \bar{\boldsymbol{\rho}}^{k+1} \rangle - \mu_2 \langle \bar{\mathbf{q}}_2^k, \bar{\mathbf{w}}^{k+1} - \Delta \bar{\boldsymbol{\rho}}^{k+1} \rangle$$

$$\geq \frac{\mu_1}{\gamma} \|\bar{\mathbf{v}}^{k+1} - \nabla \bar{\boldsymbol{\rho}}^{k+1}\|_2^2 + \frac{\mu_2}{\eta} \|\bar{\mathbf{w}}^{k+1} - \Delta \bar{\boldsymbol{\rho}}^{k+1}\|_2^2 + \|KA\bar{\boldsymbol{\rho}}^{k+1}\|_2^2,$$

18

which is equivalent to

$$-\frac{\mu_1}{\eta\gamma}\langle \mathbf{q}_1^k, \bar{\mathbf{v}}^{k+1} - \nabla\bar{\boldsymbol{\rho}}^{k+1}\rangle - \frac{\mu_2}{\eta\gamma}\langle \bar{\mathbf{q}}_2^k, \bar{\mathbf{w}}^{k+1} - \Delta\bar{\boldsymbol{\rho}}^{k+1}\rangle \tag{6.11}$$

$$\geq \frac{\mu_1}{\eta\gamma^2}\|\bar{\mathbf{v}}^{k+1} - \nabla\bar{\boldsymbol{\rho}}^{k+1}\|_2^2 + \frac{\mu_2}{\eta^2\gamma}\|\bar{\mathbf{w}}^{k+1} - \Delta\bar{\boldsymbol{\rho}}^{k+1}\|_2^2 + \frac{1}{\eta\gamma}\|KA\bar{\boldsymbol{\rho}}^{k+1}\|_2^2. \tag{6.12}$$

From (6.4) and (6.11), we have

$$\left(\frac{\mu_1}{\eta}\|\bar{\mathbf{q}}_1^k\|_2^2 + \frac{\mu_2}{\gamma}\|\bar{\mathbf{q}}_2^k\|_2^2\right) - \left(\frac{\mu_1}{\eta}\|\bar{\mathbf{q}}_1^{k+1}\|_2^2 + \frac{\mu_2}{\gamma}\|\bar{\mathbf{q}}_2^{k+1}\|_2^2\right)$$

$$\geq \frac{\mu_1}{\eta\gamma^2}\|\bar{\mathbf{v}}^{k+1} - \nabla\bar{\boldsymbol{\rho}}^{k+1}\|_2^2 + \frac{\mu_2}{\eta^2\gamma}\|\bar{\mathbf{w}}^{k+1} - \Delta\bar{\boldsymbol{\rho}}^{k+1}\|_2^2 + \frac{1}{\eta\gamma}\|KA\bar{\boldsymbol{\rho}}^{k+1}\|_2^2, \tag{6.13}$$

which indicates

$$\begin{cases} \{\bar{\mathbf{q}}_1^k : \forall k\} \text{ and } \{\bar{\mathbf{q}}_2^k : \forall k\} \text{ are bounded,} \\ \lim_{k\to\infty}\|\bar{\mathbf{v}}^{k+1} - \nabla\bar{\boldsymbol{\rho}}^{k+1}\|_2 = 0, \\ \lim_{k\to\infty}\|\bar{\mathbf{w}}^{k+1} - \Delta\bar{\boldsymbol{\rho}}^{k+1}\|_2 = 0, \\ \lim_{k\to\infty}\|KA\bar{\boldsymbol{\rho}}^{k+1}\|_2 = 0. \end{cases}$$

Together with (6.3) and definitions of $\bar{\boldsymbol{\rho}}^k, \bar{\mathbf{v}}^k, \bar{\mathbf{w}}^k, \bar{\mathbf{q}}_1^k, \bar{\mathbf{q}}_2^k$, we have

$$\begin{cases} \{\mathbf{q}_1^k : \forall k\} \text{ and } \{\mathbf{q}_2^k : \forall k\} \text{ are bounded,} \\ \lim_{k\to\infty}\|\mathbf{v}^{k+1} - \nabla\boldsymbol{\rho}^{k+1}\|_2 = 0, \\ \lim_{k\to\infty}\|\mathbf{w}^{k+1} - \Delta\boldsymbol{\rho}^{k+1}\|_2 = 0, \\ \lim_{k\to\infty}\|KA(\boldsymbol{\rho}^{k+1} - \boldsymbol{\rho}^*)\|_2 = 0. \end{cases} \tag{6.14}$$

On the other hand, the second inequality of (6.2) implies

$$\mu_1\|\mathbf{v}^*\|_1 + \mu_2\|\mathbf{w}^*\|_1 + \frac{1}{2}\|KA\boldsymbol{\rho}^* - \mathbf{d}\|_2^2$$

$$\leq \mu_1\|\mathbf{v}^{k+1}\|_1 + \mu_2\|\mathbf{w}^{k+1}\|_1 + \mu_1\langle \mathbf{q}_1^*, \mathbf{v}^{k+1} - \nabla\boldsymbol{\rho}^{k+1}\rangle + \mu_2\langle \mathbf{q}_2^*, \mathbf{w}^{k+1} - \Delta\boldsymbol{\rho}^{k+1}\rangle \tag{6.15}$$

$$+\frac{\mu_1}{2\gamma}\|\mathbf{v}^{k+1} - \nabla\boldsymbol{\rho}^{k+1}\|_2^2 + \frac{\mu_2}{2\eta}\|\mathbf{w}^{k+1} - \Delta\boldsymbol{\rho}^{k+1}\|_2^2 + \frac{1}{2}\|KA\boldsymbol{\rho}^{k+1} - \mathbf{d}\|_2^2.$$

If we take $\boldsymbol{\rho} = \boldsymbol{\rho}^*$ in (6.8), $\mathbf{v} = \mathbf{v}^*$ in (6.9), and $\mathbf{w} = \mathbf{w}^*$ in (6.10), we have

$$\mu_1\|\mathbf{v}^*\|_1 + \mu_2\|\mathbf{w}^*\|_1 + \frac{1}{2}\|KA\boldsymbol{\rho}^* - \mathbf{d}\|_2^2$$

$$\geq \mu_1\|\mathbf{v}^{k+1}\|_1 + \mu_2\|\mathbf{w}^{k+1}\|_1 + \mu_1\langle \mathbf{q}_1^k, \mathbf{v}^{k+1} - \nabla\boldsymbol{\rho}^{k+1}\rangle + \mu_2\langle \mathbf{q}_2^k, \mathbf{w}^{k+1} - \Delta\boldsymbol{\rho}^{k+1}\rangle \tag{6.16}$$

$$+\frac{\mu_1}{\gamma}\|\mathbf{v}^{k+1} - \nabla\boldsymbol{\rho}^{k+1}\|_2^2 + \frac{\mu_2}{\eta}\|\mathbf{w}^{k+1} - \Delta\boldsymbol{\rho}^{k+1}\|_2^2 + \frac{1}{2}\|KA\boldsymbol{\rho}^{k+1} - \mathbf{d}\|_2^2.$$

Together with (6.14), we have

$$\liminf\left(\mu_1\|\mathbf{v}^{k+1}\|_1 + \mu_2\|\mathbf{w}^{k+1}\|_1 + \frac{1}{2}\|KA\boldsymbol{\rho}^{k+1} - \mathbf{d}\|_2^2\right)$$

$$\geq \mu_1\|\mathbf{v}^*\|_1 + \mu_2\|\mathbf{w}^*\|_1 + \frac{1}{2}\|KA\boldsymbol{\rho}^* - \mathbf{d}\|_2^2$$

$$\geq \limsup\left(\mu_1\|\mathbf{v}^{k+1}\|_1 + \mu_2\|\mathbf{w}^{k+1}\|_1 + \frac{1}{2}\|KA\boldsymbol{\rho}^{k+1} - \mathbf{d}\|_2^2\right),$$

by taking $\liminf$ in (6.15) and $\limsup$ in (6.16). Hence, we complete the proof of (6.1).

(6.1) implies clearly that $\{\boldsymbol{\rho}^k\}$ is a minimizing sequence of $\mathcal{E}(\cdot)$. If the minimizer of $\mathcal{E}(\cdot)$ is unique, then $\boldsymbol{\rho}^k \to \boldsymbol{\rho}^*$. $\hfill\square$

We can also adapt Theorem 4.3 in [27] to get the following theorem.

Theorem 2 *Assume* $(\boldsymbol{\rho}^*, \mathbf{v}^*, \mathbf{w}^*; \mathbf{q}_1^*, \mathbf{q}_2^*)$ *be a saddle-point of* $\mathcal{L}(\boldsymbol{\rho}, \mathbf{v}, \mathbf{w}; \mathbf{q}_1, \mathbf{q}_2)$. *Suppose that the minimization problem (3.4) is roughly solved in each iteration, i.e.* $L = 1$ *in Algorithm 2. Then the sequence* $(\boldsymbol{\rho}^k, \mathbf{v}^k, \mathbf{w}^k; \mathbf{q}_1^k, \mathbf{q}_2^k)$ *satisfies*

$$\begin{cases} \lim_{k\to\infty} \mu_1 \|\mathbf{v}^k\|_1 + \mu_2 \|\mathbf{w}^k\|_1 + \frac{1}{2}\|KA\boldsymbol{\rho}^k - \mathbf{d}\|_2^2 = \mathcal{E}(\boldsymbol{\rho}^*), \\ \lim_{k\to\infty} \|\mathbf{v}^k - \nabla\boldsymbol{\rho}^k\|_2 = 0, \\ \lim_{k\to\infty} \|\mathbf{w}^k - \Delta\boldsymbol{\rho}^k\|_2 = 0, \\ \lim_{k\to\infty} \|KA(\boldsymbol{\rho}^k - \boldsymbol{\rho}^*)\|_2 = 0. \end{cases} \tag{6.17}$$

Moreover, (6.17) indicates that $\{\boldsymbol{\rho}^k\}$ *is a minimizing sequence of* $\mathcal{E}(\cdot)$. *If the minimizer of* $\mathcal{E}(\cdot)$ *is unique , then* $\boldsymbol{\rho}^k \to \boldsymbol{\rho}^*$.

Similar to the proof for Theorem 1, we can also adapt the proof for Theorem 4.3 of [27] to prove Theorem 2 here. In interest readers can consult [27].

References

[1] R. Abraham, M. Bergounioux, and E. Trelat, *A penalization approach for tomographic reconstruction of binary axially symmetric objects*, Applied Mathematics and Optimization, 58 (2008), pp. 345–371.

[2] T. J. Asaki, *Quantitative Abel tomography robust to noisy, corrupted and missing data*, Optimization and Engineering, 11 (2010), pp. 381–393.

[3] T. J. Asaki, R. Chartrand, K. R. Vixie, and B. Wohlberg, *Abel inversion using total variation regularization*, Inverse Problem, 21 (2005), pp. 1895–1903.

[4] T. Asaki, P. R. Campbell, R. Chartrand, C. E. Powell, K.R. Vixie, and B. E. Wohlberg, *Abel inversion using total variation regularization: applications*, Inverse Problem in Science and Engineering, 14(2006), pp. 873–885.

[5] R. H. T. Bates, K. L. Garden, and T. M. Peters, *Overview of computerized tomography with emphasis on future developments*, Proc. IEEE 71, 3 (1983), pp. 356–297.

[6] K. Bredies, K. Kunisch, and T. Pock, *Total generalized variation*, SIAM Journal on Image Sciences, 3 (2010), pp. 492–526.

[7] A. Chambolle, *An algorithm for total variation minimization and applications*, Journal of Mathematical Imaging and Vision, 20 (2004), pp. 89–97.

[8] T. F. Chan, A. Marquina, and P. Mulet, *High-order total variation-based image restoration*, SIAM J. Sci. Comput., 22 (2000), pp. 503–516.

[9] T. Chen and H. R. Wu, *Space variant median filters for the restoration of impulse noise corrupted images,* IEEE Trans. Circuits Syst. II, Analog Digit. Signal Process., 48 (2001), pp. 784–789.

[10] P. L. Combettes and V. R. Wajs, *Signal recovery by proximal forward-backward splitting,* Multiscale Model. and Simul., 4 (2005), pp. 1168–1200.

[11] D. Donoho, *De-noising by soft-thresholding,* IEEE Transactions on Information Theory, 41 (1995), pp. 613–627.

[12] H. L. Eng and K. K. Ma, *Noise adaptive soft-switching median filter,* IEEE Trans. Image Process., 10 (2001), pp. 242–251.

[13] T. GOLDSTEIN AND S. OSHER, *The split Bregman method for L1 regularized problems,* SIAM Journal on Imaging Sciences, 2 (2009), pp. 323–343.

[14] K. M. Hanson, *A Bayesian approach to nonlinear inversion: Abel inversion from X-ray attenuation data, maximum entropy and Bayesian methods in applied statistics,* edited by J. H. Justice, Cambridge University Press, Cambridge, England, 1986.

[15] J.-B. Hiriart-Urruty and C. Lemaréchal, *Convex analysis and minimization algorithms,* Springer-Verlag Berlin, **I**, 1996.

[16] H. Hwang and R. A. Haddad, *Adaptive median filters: new algorithms and results,* IEEE Trans. Image Process., 4 (1995), pp. 499–502.

[17] F. Knoll, K. Bredies, T. Pock, and R. Stollberger, *Second order total generalized variation (TGV) for MRI,* Magnetic Resonance in Medicine, 65 (2011), pp. 480–491.

[18] S. Kontogiorgis and R. R. Meyer, *A variable-penalty alternating directions method for convex optimizations,* Mathematical Programming, 83 (1998), pp. 29–53.

[19] M. Lysaker, A. Lundervold, and X.-C. Tai, *Noise removal using fourth-order partial partial differential equation with applications to medical magnetic resonance images in space and time,* IEEE Trans. Image Process., 12 (2003), pp. 1579–1590.

[20] M. Lysaker and X.-C. Tai, *Iterative image restoration combining total variation minimization and a second-order functional,* International Journal of Computer Vision, 66 (2005), pp. 5–18.

[21] M. Nikolova, *Local strong homogeneity of a regularized estimator,* SIAM J. Appl. Math., 2(2000), pp. 633–658.

[22] P. E. Ng and K. K. Ma, *A switching median filter with boundary discriminative noise detection for extremely corrupted images,* IEEE Trans. Image Process., 15 (2006), pp. 1506–1516.

[23] R. Rockafellar, *Monotone operators and the proximal point algorithm.* SIAM Journal of Control and Optimization, 14 (1976), pp. 877-898.

[24] L. Rudin, S. Osher, and E. Fatemi, *Nonlinear total variation based noise removal algorithms,* Physica D., 60 (1992), pp. 259–268.

[25] A. N. Tikhonov and V. Y. Arsenin, *Solution of ill-posed problems,* New York: Wiley, 1977.

[26] C. L. Wu and X. C. Tai, *Augmented Lagrangian method, dual methods, and split Bregman iteration for ROF, vectorial TV, and high order models*, SIAM J. Imaging Science, 3(2010), pp. 300–339.

[27] C. L. Wu, J. Y. Zhang, and X. C. Tai, *Augmented Lagrangian method for total variation restoration with non-quadratic fidelity*, Inverse Problems and Imaging, 5(2010), pp. 237–261.

[28] X. C. Tai and C. L. Wu, *Augmented Lagrangian method, dual methods and split Bregman iteration for ROF model, Scale Space and Variational Methods in Computer Vision, Second International Conference*, SSVM 2009, Voss, Norway, June 1-5, 2009. Proceedings. Lecture Notes in Computer Science 5567 (2009) , Springer, pp. 502–513.